Extracted from :

SIMULATION OF LIDAR RETURNS FROM PRISTINE AND DEFORMED HEXAGONAL ICE PRISMS IN COLD CIRRUS BY MEANS OF "FACE-TRACING"

Massimo Del Guasta

J. Geophys. Res. Vol. 106 ,D12 , 12589-12602, 2001.

Istituto di Ricerca sulle Onde Elettromagnetiche (IROE) - CNR , Via Panciatichi 64, 50127

Firenze, Italy

ABSTRACT.

The simulation of the optical properties of ice clouds plays a crucial role in the interpretation of remote sensing data of cirrus clouds. In this work, a novel simulation code ("Face-tracing") derived from ray-tracing was described and used to compute LIDAR depolarization and the extinction/backscatter ratio at 532 nm, as expected from randomly-oriented pristine and slightly deformed hexagonal prisms of various sizes and aspect ratios. By increasing the aspect ratio, the depolarization of pristine crystals was found to increase sharply from 0 (thin plates) to a maximum value (columns) at an aspect ratio of around 1, where an absolute minimum of extinction/backscatter ratio (corresponding to a maximum LIDAR backscatter efficiency) was also found. When including the far-field diffraction in backscattering simulations, pristine particles smaller than 100 μm showed depolarization and extinction/backscatter ratios comparable with the experimental LIDAR data of cold (T<30°C) polar cirrus. Recent in-situ observations showed the widespread presence of non-pristine hexagonal crystals in cirrus, stimulating the calculation of the backscatter properties of deformed particles by "face-tracing". Simulations for deformed hexagonal prisms showed in most cases a smaller depolarization and a higher extinction/backscatter ratio compared with those obtained for pristine crystals. A mixture containing variable proportions of pristine and deformed hexagonal prisms (with an aspect ratio of 1-2) resulted in a depolarization-extinction/backscatter scatter plot similar to the experimental one for cold polar cirrus.

INTRODUCTION.

The elastic-backscatter LIDAR is a powerful remote-sensing tool that produces vertical, 2-D, or 3-D qualitative maps of the distribution of aerosol backscatter in ice clouds. Even if LIDAR spatial and temporal resolutions are high enough to obtain an accurate map of aerosol backscatter, the precision and accuracy of the microphysical aerosol information derived are usually affected by large uncertainties. This is due to the strong variability of ice-particle shapes and size distributions, which makes it difficult to define a general model for the backscatter properties of ice clouds. In the last decades, the development of powerful computers has made it possible to compute numerically the scattering properties of particles of a complex shape. Most simulations of cirrus optical properties have been carried out by means of ray-tracing techniques, in the hypothesis that ice particles larger than the wavelength dominated the size spectrum. Pristine hexagonal crystals were extensively used in earlier simulations (Cai and Liou, 1982; Takano and Jayaweera, 1985; Takano and Liou, 1989; Muinonen et al., 1989; Hess and Wiegner, 1994; Zhang and Xu, 1995). The use of pristine hexagonal crystals in simulations make it possible a correct prediction of the halos observed in some cirrus. But halos are observed seldom in nature, and direct replicas of cirrus particles often show non-pristine crystals (Konnen *et al.*, 1994). The fact that optical properties of ice crystals do not agree with simulations with ideal ice particles has triggered the modeling of light scatter by more realistic, irregular ice particles. Particle aggregates such as bullet rosettes (Iaquinta *et al.*, 1995), polyedral particles of different shapes (Takano and Liou, 1995; Macke, 1993), and deformed hexagonal crystals (Macke et al., 1996; Hess *et al.* , 1998) were modeled. In recent years, some fractal shapes were also simulated using ray-tracing techniques (Macke et al., 1996; Mishchenko *et al.*, 1996). Unfortunately, most ray-tracing simulations performed on ice crystals are not devoted to the LIDAR community, and the scattering quantities derived from these works cannot be easily compared with LIDAR data-sets.

In this work, a novel geometric optics (GO) technique called “face-tracing” and derived from normal ray-tracing techniques is described and used to compute the LIDAR depolarization and the extinction/backscatter ratio for a wide range of pristine and deformed hexagonal crystals randomly oriented in space. With this technique it is possible to calculate the exact size and shape of the individual beams backscattered by polyhedral ice crystals,

making possible to calculate the contribution of diffraction to the LIDAR backscatter. Results are discussed in comparison with a LIDAR data-set of cold (T<-30°C) polar cirrus.

METHODS.

"Face-tracing" (FTR) is a numerical technique developed at IROE, and is derived from ray-tracing. The technique permits the scattering to be simulated for convex, polyedral particles of an arbitrary shape bounded by flat surfaces. In this work, pristine and slightly deformed hexagonal crystal randomly oriented in space were considered.

Each flat face of the polyhedral particle (e.g. the hexagonal crystal of Fig.1, defined by its length "l" and side "a") was parameterized by its vertices. The crystal was rotated in space by using the geometry shown in Fig 1. The LIDAR light, linearly polarized along the x axis, was sent vertically along the z direction. In order to simulate random 3-D particles, the angles ϕ and υ were step-varied with a step of 0.5° each. Only two γ values (0° and 90 °) were used, as these were sufficient for computing the scattering for random 3-D particles (Del Guasta, 1995). For the optical simulations, I assumed the refractive index of ice at 532 nm (Warren, 1984), disregarding the negligible, imaginary part. The birefringence of ice was disregarded, as its effect on depolarization and the phase function is negligible (Takano and Liou, 1989). The interference between emerging "rays" was also disregarded.

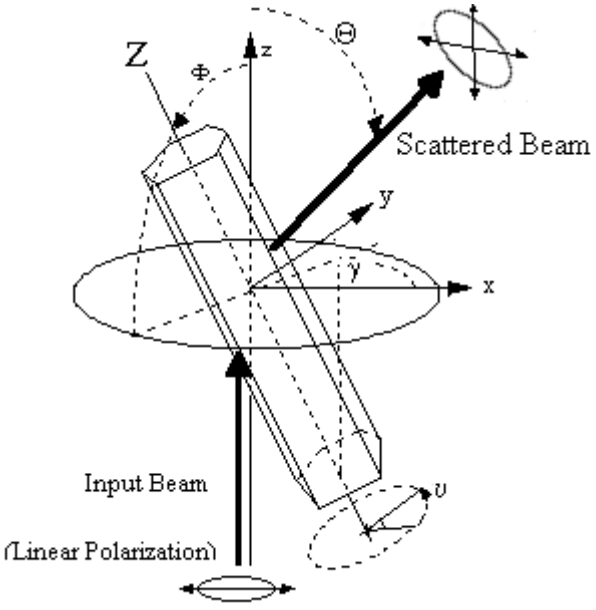

Fig. 1: The scattering geometry adopted in the FTR technique

By using conventional ray-tracing techniques, single rays are traced into the particle, and the scattered energy is collected into solid angle intervals at different scattering angles so as to reconstruct the phase function. With the FTR technique, each face of the crystal illuminated by the LIDAR defines an initial finite beam that replaces the set of rays that illuminated the same face when the conventional technique was used. The projection of each face along the direction of the laser beam (z axis) defines the cross-section of the initial beam. The total power impinging the initial face is computed as the product of the light intensity and the cross-section of the beam. The initial beam is reflected and refracted onto the "initial" face: the direction and the electric-field vector of the reflected and refracted beams are computed with the usual Snell and Fresnel laws (Cai and Liou, 1982). The cross section of the beam reflected in space is computed by projecting the reflecting face along the reflected beam; the reflected power is computed as the product of the reflected intensity and the beam cross-section. When proceeding within the particle, the refracted beam hits some faces of the solid internally, and is thus split into several sub-beams, one for each of the faces encountered. The intersection between the refracted beam and each encountered face is numerically computed, and the projection of this intersection along the refracted beam defines a new "sub-beam", which will be later reflected and refracted (or totally reflected) by the encountered face. The intersections between beams and faces are obtained numerically. In the simplest cases, the intersection is completely contained inside the encountered face, or the face is completely contained within the beam projection. In these cases, the cross section of the sub-beam is determined by the beam cross-section itself or by the projection of the face along the beam direction, respectively (Fig. 2a and Fig.2b). In other cases, the intersection between the beam and the face is a polygon, the vertices of which can be obtained numerically from the vertices of the projection and those of the face (Fig. 2c). This process is repeated for all the faces illuminated by the refracted beam, thus creating a sub-beam for each illuminated face.

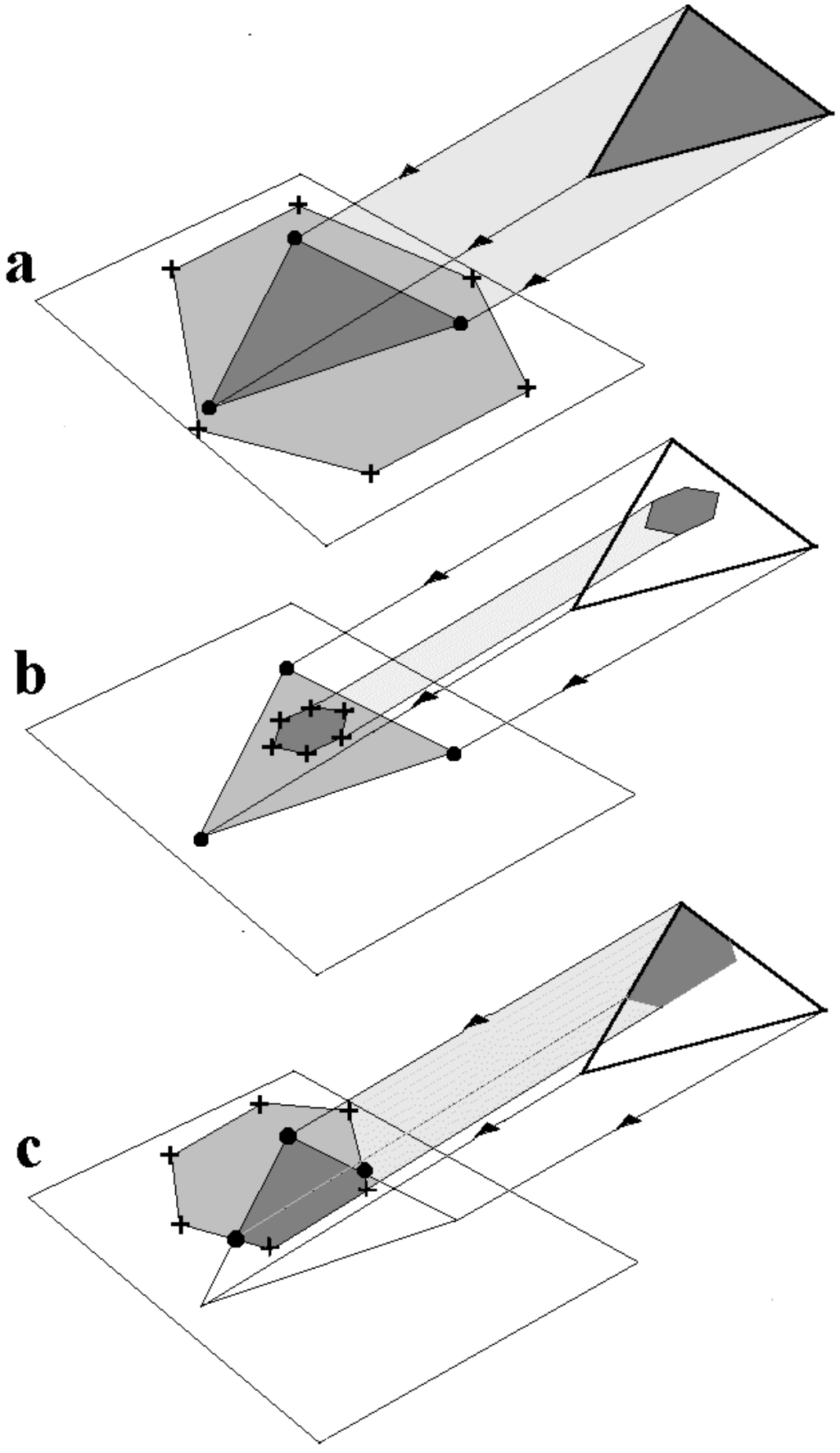
a
b
c

Fig.2: The production of a sub-beam: a beam (of triangular section) hits on the plane containing a hexagonal face. The illuminated part of the face defines a new sub-beam (dark grey). a) The beam projection (circles) is contained within the face (crosses); b)The face is contained inside the beam projection; c) The intersection of the beam projection and the face is a polygon, the vertices of which are obtained numerically from the vertices of the face and of the projection.

The sum of the powers of the sub-beams must be equal to the power of the original beam. If not, an error in the beam-splitting process occurred, because an "insoluble geometrical" situation was found. This situation usually occurs (in less than 1% of cases) when the incident beam almost skims the illuminated face, or when the shape of the beam-face intersection is too complex to be managed by the code. In these cases, the successive production of higher-order sub-beams is aborted.

Each sub-beam created by the code undergoes the same process as the initial beam, by producing a reflected and a refracted beam (or just a totally reflected beam). The beam-splitting process continues until a fixed amount (R'=99.5%) of the energy impinging on each initial illuminated face of the solid has been scattered in space. In order to reduce the computing time, the maximum number of internal reflections was limited to 10 (plus the number of total internal reflections). The process is repeated for all the illuminated faces of the crystal: the number of input beams replacing the optical rays of the conventional ray-tracing techniques was reduced to the number of faces of the solid illuminated by the laser beam. The total number of optical computations was thus reduced, even if the splitting of the beams into a great number of sub-beams required much more geometrical computing than when using the conventional technique. FTR resulted in a reduction of the computing time by a factor 4 with respect to a conventional ray-tracing technique that had previously been implemented at IROE (Del Guasta, 1995). Another advantage of FTR is its ability to compute exactly the shape and the normal section of any scattered beam, which in turns makes it possible to compute the diffraction associated with each emerging beam.

The conservation of power during the production of higher-order sub beams is an indicator of the efficiency of the process: at the end of the simulation, a fraction R' of the total power impinging on the crystal should be scattered all around, and any error in the beam-splitting procedure results in a smaller ratio R<R'.

The light backscattered to the "LIDAR" during the process was collected into cones with a common axis at Θ=180° with 1,5,10,50, and 100 mrad half-apertures. The half-aperture of the cone will be referred to as the "Averaging Cone" (AC) in the rest of this work. The backscattering coefficients (differential cross sections at Θ=180°) parallel (βp) and perpendicular (βs) to the laser polarization were computed separately for different AC. The LIDAR depolarization in this work is defined as: $\delta = \frac{\beta_s}{\beta_s + \beta_p}$. Another important LIDAR-derived quantity, the ratio (k) between the extinction cross section (σ) and the total backscattering coefficient was also computed: $k = \frac{\sigma}{\beta_s + \beta_p}$ (units for k are [sr]).

The GO part P_{g11} of the phase function P_{11} (the solid angle normalization of the first component of the Stokes matrix) was computed by collecting the scattered light in the Θ∈[0 180 °] range, with a collecting resolution of ΔΘ= 1 °. The forward, transmitted peak obtained by GO was treated separately from the rest of the scattered radiation, and was not included in the normalization factor of P_{11}, as suggested by Takano and Liou (1989).

As obtained by ray-tracing, P_{11g} , δ and k are size-independent. The size-dependent forward diffracted part P_{11d} of the phase function was computed by smoothing out the Fraunhofer diffraction oscillations, by assuming a uniform distribution of isomorphic crystals with rectangular size distribution $0.7 \cdot l < l' < 1.4 \cdot l$. Forward diffraction was simulated by considering a circular aperture of diameter $D = \sqrt{\frac{S}{\pi}}$ where S is the total surface of the particle. These assumptions were used to smooth the diffraction phase function P_{11d}, and had no effect in the rest of the LIDAR simulations. The forward diffraction lobe was added to the phase function obtained by ray-tracing in order to obtain the phase function $P_{11} = (P_{11g} + P_{11d})/2$ (Takano and Liou, 1989) to be compared with the results of conventional ray-tracing codes. The extinction cross section (σ) was assumed to be twice the GO extinction (Van de Hulst, 1957), in order to account for the forward diffraction. A comparison of P11 as computed by FTR with the ray-tracing results of Takano and Liou (1989) for a crystal of l=200 μm, a=40 μm showed a good agreement, with a maximum relative difference of 11% for any angular bin over the whole Θ∈[0 180 °] scattering angle range.

RESULTS FOR PRISTINE HEXAGONAL CRYSTALS.

FTR was extensively used to simulate δ and k for pristine, hexagonal ice crystals with different aspect ratios (AR), defined as: $AR = \frac{l}{2a}$.

All simulations were carried out at 532 nm, assuming linearly-polarized incoming light. Several simulations were performed for the same AR using different (a,l) pairs, in order to estimate the effect of the size-dependent approximations of the code involved in the final results. The ratio R between the GO extinction cross section and the theoretical cross section was computed for any simulated crystal in order to assess the overall "energy loss" caused by numerical truncation an by the "insoluble" geometrical problems encountered by the code. Theoretically, the GO cross section is equal to S/4. If the number of "insoluble" cases encountered by the code is negligible, R is close to R'. The ratio R/R' resulted in the $0.95<R/R'<1$ range for $0.1<AR<100$, meaning that a maximum energy loss of 5% was introduced by the software. In the case of usual plates/columns ($0.1<AR<10$), in 80% of insoluble cases the FTR routine aborted when the total energy diffused by the crystal differed less than 4% from the input one. The analysis of the crystal orientations at which insoluble geometrical problems occurred showed that this type of error can occur for any (ν, ϕ) orientation, with an almost random distribution in the (ν, ϕ) space. Even if it is impossible to define with precision an error for each FTR-simulated bin of the phase function (the missing contribution of aborted beams to each P_{11} bin is obviously unknown), this analysis ensures that the relative error on P_{11} due to "insoluble cases" is almost uniformly distributed throughout the whole phase function, and is of the order of 4-5%. The same error affects βp and βs, and the relative error on δ is thus expected to be of the order of 10% ($0.1<AR<10$). In the case of very long columns ($10<AR<100$), in 80% of insoluble cases the FTR routine aborted when the total energy diffused by the crystal differed less than 12% from the input one, and the maximum relative error on depolarization is thus of the order of 25%.

Results for depolarization were plotted for different AC as a function of AR (Fig.3). For $AR<0.2$ (thin plates), LIDAR depolarization is very small ($\delta<<5\%$) for any AC. δ increases sharply for $0.2<AR<1$, and becomes

relatively constant for 1<AR<10 and AC<100 mrad . In the 1<AR<10 region, depolarization branches into very different values, depending on AC. The smaller the AC, the higher the depolarization. The depolarization is roughly comprised between 40-60% (AC=1 mrad) and 26% (AC=100 mrad) for 1<AR<10.

Results for AC =10-50 mrad were compared with the results of Takano and Jayaweera (1985), obtained with a collecting angle $\Delta\Theta=2°$ and similar AR: depolarization for columns agreed with the reference data (within 2% absolute error), while depolarization of plates was lower in the present work (16% against 26% of Takano and Jayaweera ,1985). A good agreement was found with Takano and Liou (1995) and with the simulations of Hess et al. (1998): by simulating almost pristine hexagonal crystals at 550 nm, these authors found a quite constant $30\%<\delta<34\%$ for 1.3<AR<6, to be compared with the range $27\%<\delta<39\%$ (AC>1 mrad) obtained in this work (Fig.3)

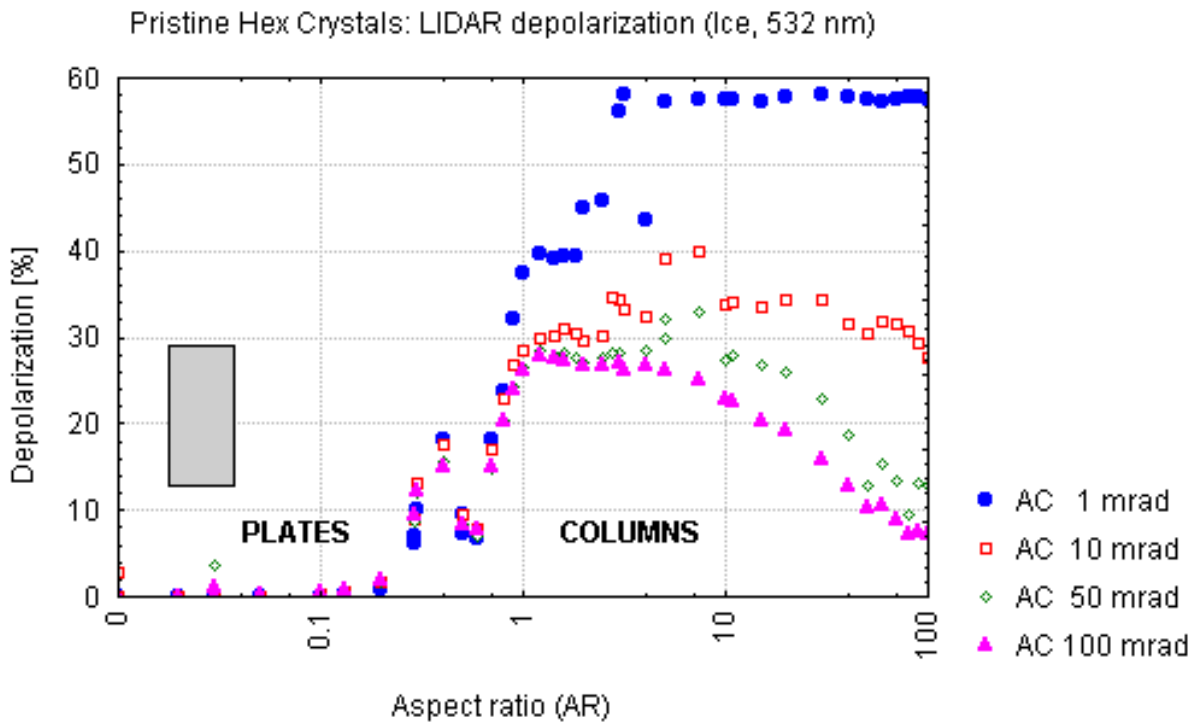

Fig.3 : δ results for pristine crystals. Results for different AC are shown as functions of AR. The range of δ values observed in Antarctic cold cirrus (T<-30°C) by Del Guasta *et al.*(1993) are shown as a gray bar.

The interpretation of Fig.3 requires the identification of the spatial orientations of the crystals that contribute to the backscatter. In Fig.4a and Fig4b the parallel backscatter βp and the depolarization δ associated with the backscattered beams are shown as functions of the spatial rotations ν and ϕ defined in Fig.1. The (ν,ϕ) pairs

leading to backscatter (Fig 4a) form a peculiar "Ψ" pattern with branches corresponding to different light paths within the crystal. The "A" branch originates from specular reflections. Branch "B" includes a wide range of "ray-paths": at low ϕ angles, simple paths are possible in which rays impinging a basal or a lateral face are refracted into the crystal and back-reflected to the first face after reflection on a basal face and a reflection on a lateral face ("plane skew rays" in the notation of Takano and Jayaweera (1985)). These paths originate the "foot" of the "B" branch. The rest of the "B" branch originates from simple paths in which the ray hits a lateral face, is internally reflected by a basal face and a lateral one, and finally emerges as a backscattered ray from another lateral face ("spatial skew rays" in the notation of Takano and Jayaweera (1985)). "B" branch ($20°<\phi<40°$) produces most of the backscatter for a very narrow range of ν ($\nu\approx30°$, the ν angle at which, for $\phi=0$, pairs of lateral faces are perpendicular to the laser light). A corner-reflector effect occurs in these conditions (Borovoi, 1999; Del Guasta, 1999). The backscattered light is strongly depolarized ($\delta>50\%$) in the central part of branch B. The light is moderately depolarized ($0\%<\delta<30\%$) in the upper part of the "B" branch, in which the long axis of the crystal is almost perpendicular to the laser light. The B branch determines backscatter and depolarization for pristine, hexagonal crystals. In branch "C", backscatter is produced by a short path within the crystal: the ray hitting a lateral face is reflected once or twice by the lateral faces, and reflected an odd number of times on the basal faces ("spatial skew rays"). This type of path produces small depolarization. A larger depolarization, but a small backscatter, is produced in branch "D", which corresponds to complex and long ray-paths (spatial skew rays) involving a large odd number of reflections on the lateral faces. The effect of increasing AC on the backscattered light is evident in Fig.4: the number of crystal orientations generating backscattered radiation increases markedly for AC=100 mrad , but most of the new orientations produce a small depolarization. As a consequence, an overall depolarization decrease occur when increasing AC (Fig.3). In the case of thin plates, the depolarized branch D does not exists, and the strongest (depolarized) part of branch B is depleted. In plates, most backscatter derives from branch A and from the weakly depolarized branch C. As a result, (already pointed out by Takano and Jayaweera (1985)), LIDAR depolarization is much smaller in plates than in columns, explaining the depolarization increase with AR shown in Fig.3. Another feature of Fig.3 is the decreasing trend of depolarization when increasing AR at large AC. As shown in Fig.4, a gradual thickening of all the branches of the "Ψ" plot occurred when AC was increased. In the case of large AR, the thickening did not occur in

branch D. This effect was caused by the small probability that a light ray could follow the long and complex path within the crystal (a characteristic of branch D) and emerge as a backscattered ray. The relative thinness of the depolarized branch D, compared to the other branches, explains the decreased depolarization observed in Fig.3 for long columns with large AC.

From plots like those in Fig.4, it is also possible to estimate the LIDAR properties of horizontally-oriented ice crystals, that are often encountered in cirrus. Since most depolarized backscatter is produced in the B branch, horizontally-oriented plates ($0.01<AR<1$) with a maximum tilt angle ϕ of 10° would produce a nearly-zero depolarization for any AC (Fig.4). Plate depolarization increases up to the random 3-D values when the maximum tilt angle ϕ is increased above $\phi \approx 60°$. In the case of columns, horizontal orientation means $\phi \approx 90°$. Also in this case, the depolarization produced by columns ($1<AR<50$) the major axis of which is horizontally oriented within a ±20° tilt angle is very small ($\delta << 5\%$) for any AC<200 mrad. These considerations show that a pure population of horizontally-oriented pristine crystals ($0.1<AR<10$, AC<200 mrad) cannot explain the relatively large depolarization values observed in most polar cirrus (Fig.7). For this reason, in the rest of this work, only randomly-oriented particles will be considered.

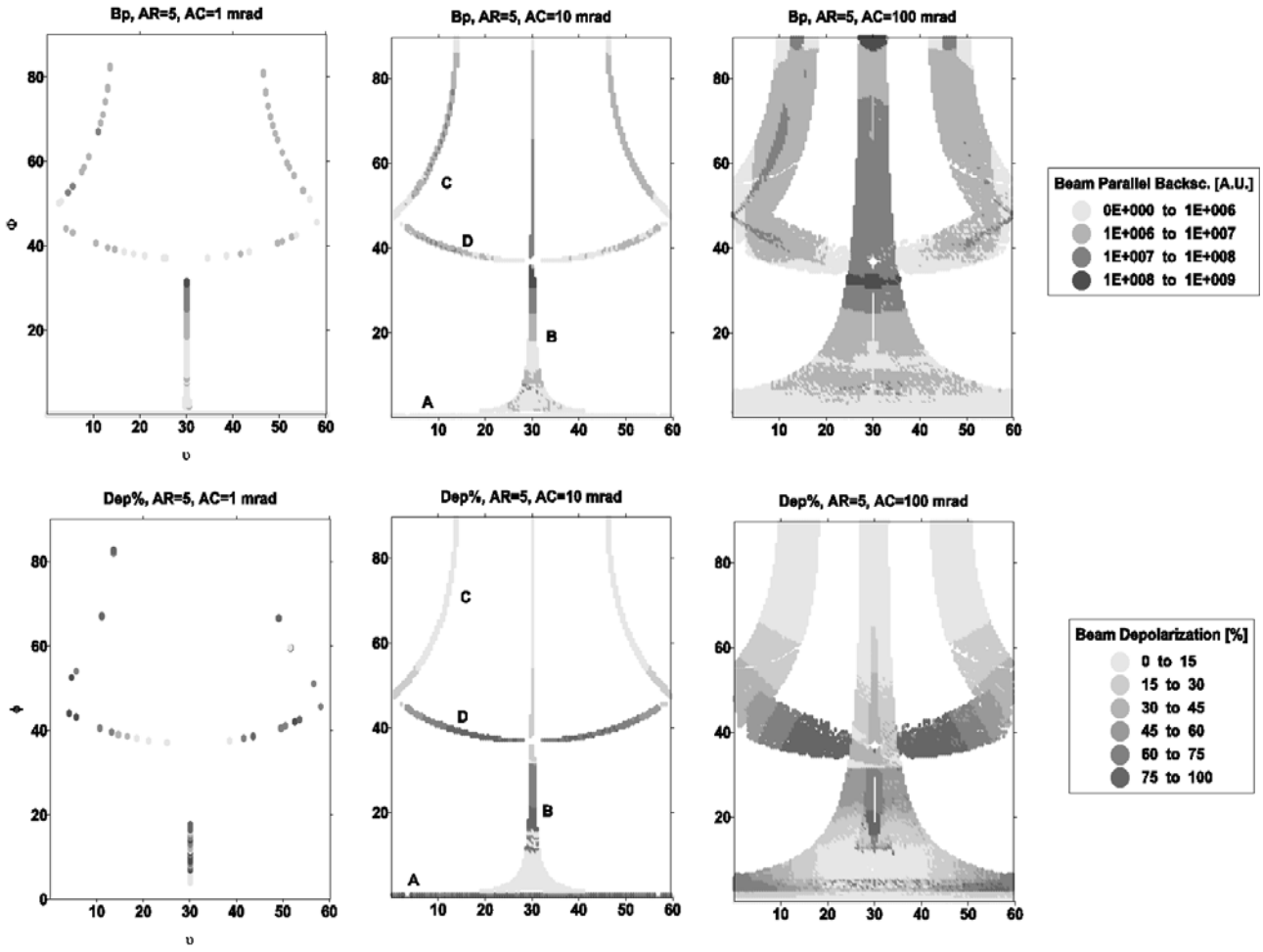

Fig.4: The spatial orientations of pristine hex crystals that originate backscatter (a) and depolarization (b) in a pristine column (AR=5), for increasing AC. The different "branches" described in the text are marked (the unexpected, high depolarization for AC=10 mrad, ϕ=0.5° is associated with very weak backscattered beams, and is practically cancelled by the 100 times intense, specular reflection occurring at ϕ=0°).

The results of k simulations for pristine crystals (Fig.5) showed a relative minimum at AR=1 for any AC. The observed k minimum shows that, for the same σ (same S), the maximum backward energy transfer occurs in "compact", cube-like hexagonal particles. Thin plates and long columns show a reduced backscatter because of the reduced extent of lateral faces and base faces, respectively. These results indicate that, in a population of hexagonal ice crystals of similar σ, particles with an unitary AR are the main contributors to the LIDAR backscatter and depolarization.

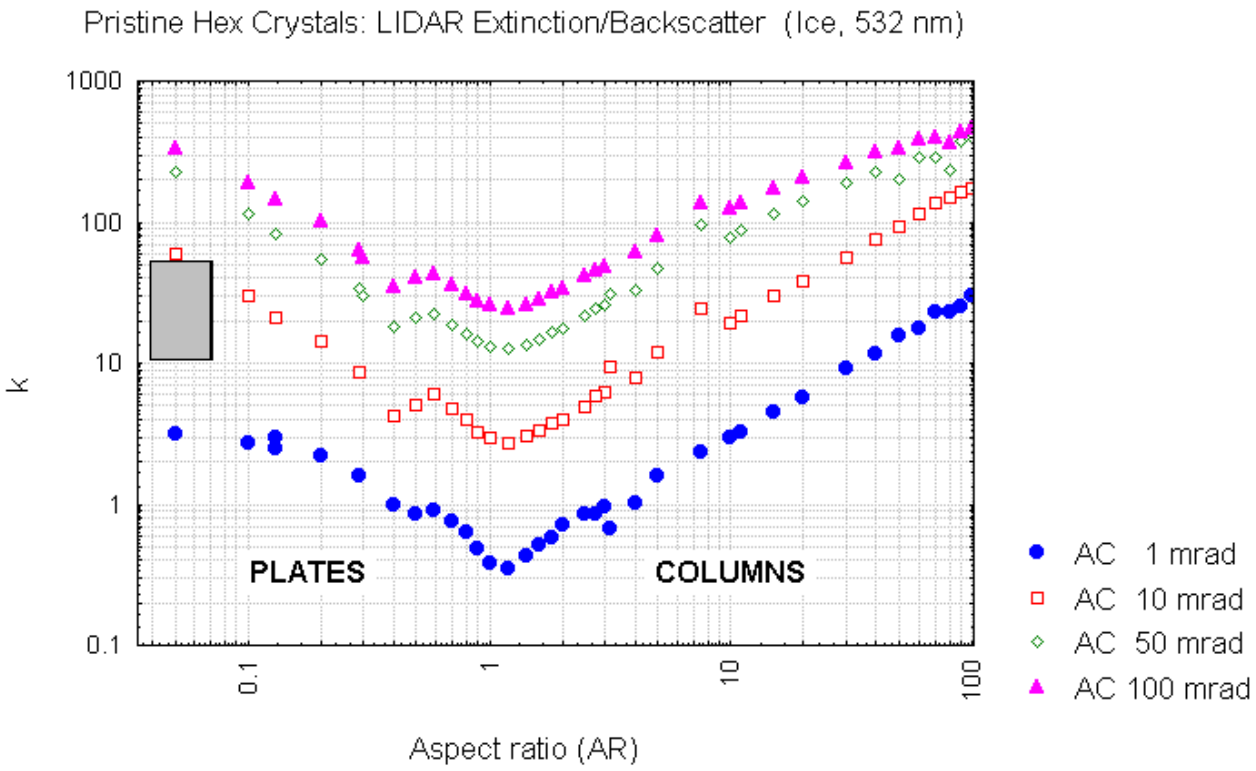

Fig.5 : k results for pristine crystals. Results for different AC are shown as functions of AR. The range of k values observed in Antarctic cold cirrus (T<-30°C) by Del Guasta *et al.*(1993) are shown as a gray bar.

The use of different AC values in FTR simulations is important, because there is a close correspondence between AC and the particle size. Because of diffraction, each finite light beam scattered by the crystal in space by GO is actually spread into a Fraunhofer principal lobe whose half-peak aperture AC in radians is $AC = \frac{0.51 \cdot \lambda}{D}$ (Van de Hulst, 1957), where D is the equivalent diameter of the normal section (in μm) of the backscattered beam (at 532 nm, $AC = \frac{0.27}{D}$). Diffraction produces a smoothing of the backward peak of the phase function: even if the LIDAR receives from a cirrus the radiation backscattered precisely at 180°, (within a solid angle of the order of 0.1 mrad for a cirrus measurement), the received radiation must be simulated by convolving β_S and β_P with the diffraction spreading function. If a relation between the normal section of the backscattered beams and the physical dimensions of crystal is known, it will be possible to relate the aperture of the spreading function with the particle size. This process was achieved by means of FTR, since the

normal section of the each backscattered beam is precisely known. For each simulated AR and AC, it was possible to compute the equivalent diameter $<D_\beta>$ of all the beams backscattered by the crystal using :

$$< D_\beta >= \sqrt{\frac{4}{\pi}\frac{\sum_i (\beta_{pi} + \beta_{si}) * D_i}{\sum_i (\beta_{pi} + \beta_{si})}}$$

where the summations are extended over all the backscattered beams received within the AC. $<D_\beta>$ was computed for pristine crystals of different AR, and the results were normalized to the crystal diameter 2a. Fig.6 shows that for AC=1 mrad the equivalent diameter for AR>1 is a fixed percentage (~ 30%) of 2a. This means that the corner-reflector effect of pristine columns is limited by the base surface of crystal and that only the crystal tips of columns contribute significantly to the backscatter, as already observed by Borovoi (1999). For thinner plates, $<D_\beta>$ converges to 2a, showing that the backscatter is limited by the base surfaces. In the case of larger ACs, also the lateral faces of long columns contribute to the backscatter (fig.6).

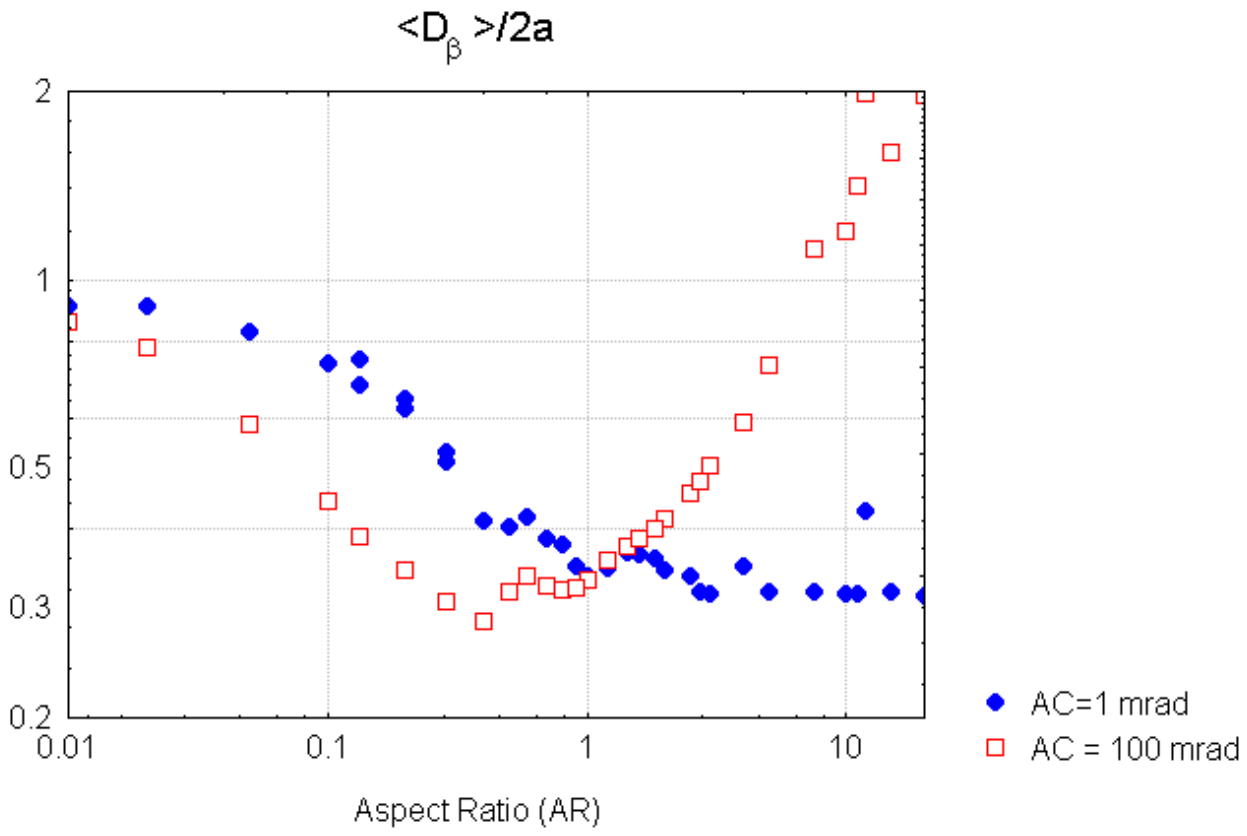

Fig 6: The ratio $<D_\beta>/2a$ plotted as a function of AR shows that for small AC the cross section of the backscattered beams is limited by the bases of the crystal.

For AR close to 1 the half-peak aperture of the first diffraction lobe of backscattered radiation could be written as: $AC \approx \frac{0.8}{2a}$. For thin plates (AR<0.5) and for columns (1<AR<10) we can write $\frac{0.27}{2a} < AC < \frac{0.8}{2a}$. These relations connect the physical dimension of the hexagonal base of the particle with the angular spreading of the backscattered radiation due to diffraction.

In cirrus clouds, particle size is comprised between a few μm and a few mm (Pruppacher and Klett, 1978). Recent measurements performed in cirrus (Heymsfield,1986; Platt *et. al*., 1989; Sassen, 1991; Arnott et al., 1993; Heymsfield and McFarquhar, 1996) showed that small ice particles (l<100 μm) are common in cold cirrus, and can dominate the size spectrum. By using a combined photometric-LIDAR technique in cold, subvisual and corona-producing cirrus, Sassen et al. (1989) and Sassen (1991) derived the size of the ice crystals involved (equivalent diameter 12-30 μm), suggesting also that AR was close to unit. Even if the presence of small ice crystals is widely accepted, the relative numerical importance of ice particles smaller than a few tens of microns is still uncertain, since the FSSP probes normally used for the sizing of small particles are known to give uncertain results in ice clouds (Platt and Spinhirne, 1989; Macke, 1993). Despite this problem, several works have pointed out the presence of large amounts of ice particles with diameters smaller than 10-20 μm in cold cirrus by means of FSSP instruments (Platt and Spinhirne, 1989). Recent works (Arnott et al., 1994; McFarquhar and Heymsfield, 1996; McFarquhar et al., 1999) have confirmed, furthermore, that the number size distributions of high cirrus particles are peaked around a diameter of 10 μm, or even less (Ström et al., 1997). The size distribution often resulted bimodal, with a second peak at a diameter of 200-600 μm. In situ replicas showed that the largest particles in cold cirrus are often rosettes of columnar crystals. Fortunately, the scattering properties of rosettes are almost identical to those of the individual (hexagonal) branches (Macke, 1993; Iaquinta et al., 1995), so that the scattering properties of complex crystals are not determined by their overall size and shape, but by the size and shape of their smaller branches. This result suggests that, even if 200-600 μm rosettes are present in cirrus, their scattering properties are similar to those of columnar crystals with a length of 100-300 μm (in principle, backscatter

properties of rosettes could not follow this simple “rule”, but a rosette branch is basically a hexagonal column with a deformed tip, and it will be shown in this work that δ and k are in this case close to those obtained for the pristine crystal).

The relative importance of the two ice crystal modes is crucial in LIDAR simulations. For a fixed crystal shape and AR, large particles show a GO extinction cross section proportional to the square of the length, and thus large particles are very efficient in producing LIDAR returns. Large particles also produce a narrow diffraction lobe in the backscatter.

The quantitative measurements of ice particles in the 1-20 μm range are still fragmentary, but most available results show that their modal concentration is 1 to 3 magnitudes larger than the modal concentration of large particles (equivalent diameter 100-400 μm). Large particles are scarce in high cold cirrus (Heymsfield and McFarquhar, 1996; McFarquhar et al., 1999), and were found to be absent in the young cold cirrostratus studied by Ström et al. (1997). In order to dominate the LIDAR backscatter, the concentration of small particles must be at least 100 times the concentration of the 10-times-larger particles. This condition is apparently verified in high cold cirrus (Arnott et al., 1994; McFarquhar et al., 1999; Ström et al., 1997), and the size distribution can be thus considered monomodal for FTR simulations.

The convolution of the GO phase function around Θ=180° with the diffraction-spreading function of the backscattered beams makes it possible to compute the correct AC to be used for computing δ and k. The convolution integral was approximated by Muinonen (1989) for different polyhedral particles of a generic size. If $<D_\beta>$ is much smaller than 100 μm, the first diffraction lobe is much wider than the aperture of the GO backscatter peak (this peak behaves as P_{11}~1/sin(θ–180°$|$) and decreases by a factor 1/e within a few mrads from Θ=180°). In this case, the convolution could be replaced with a simple average of the phase function over a cone, the semi-aperture of which is assumed to be equal to the half-peak aperture of the spreading function (AC) . If particles of a 10-100 μm size are considered, AC is in the 100-10 mrad range. This approximation was tested numerically by comparing the exact results of the convolution with the averaged values of k and δ For this test, the phase functions obtained by FTR for 0.5<AR<10 were convoluted with the diffraction spreading functions calculated for particles with 1 μm<2a<100 μm. The results of the convolutions were compared with the results of a simple averaging of the phase function over the

half-peak aperture of the spreading function. Approximated results showed a maximum absolute error of the order of 3% for δ, and a maximum relative error of 15% for k, when compared with the exact results. The averaging of the backscatter over cones of apertures AC has thus been adopted in the rest of this work for simulating, by means of FTR, the LIDAR returns of pristine crystals of different size. The approximation holds if 2a is smaller than about 100 μm (this means that the maximum dimension of the particle should be smaller than 100 μm in small plates (with a typical AR<0.5, Auer and Veal, 1970), and smaller than about 100-200 μm in small columns (with a typical AR of 1-2 (Auer and Veal, 1970; Heymsfield and Knollenberg, 1972).

COMPARISON OF SIMULATIONS FOR PRISTINE CRYSTALS WITH LIDAR DATA OF COLD POLAR CIRRUS.

Two Nd-YAG LIDARs (532 nm) run by IROE were operated in polar regions. One system is permanently installed in Dumont d'Urville (60°S, Antarctica); the other was installed at Södankyla (66°N, Finland) in 1991-1993. The large LIDAR data sets of cirrus clouds obtained at the two polar sites were processed, deriving statistics on δ and k as functions of the midcloud temperature (Del Guasta et al.,1993; Del Guasta et al.,1994). Statistics on δ and k for Antarctic clouds relevant for this work are reported in Fig.7 and Fig.8. Results for Arctic cirrus are extremely similar to Antarctic data, and were not plotted. In Fig. 7 and 8, histograms of δ and k were plotted for cold (T<-30°C) cirrus. The histogram of k values is partially broadened by the large uncertainties involved in the retrieval of this parameter from LIDAR data (Del Guasta, 1998).

Cold cirrus show a narrow range of crystal habits, compared with warmer cirrus (Pruppacher and Klett, 1985; Macke, 1993). Small, simple-shaped and almost pristine hexagonal crystals are more common in cold cirrus than in warmer cirrus, enabling a comparison of LIDAR data with the simulations performed in this work.

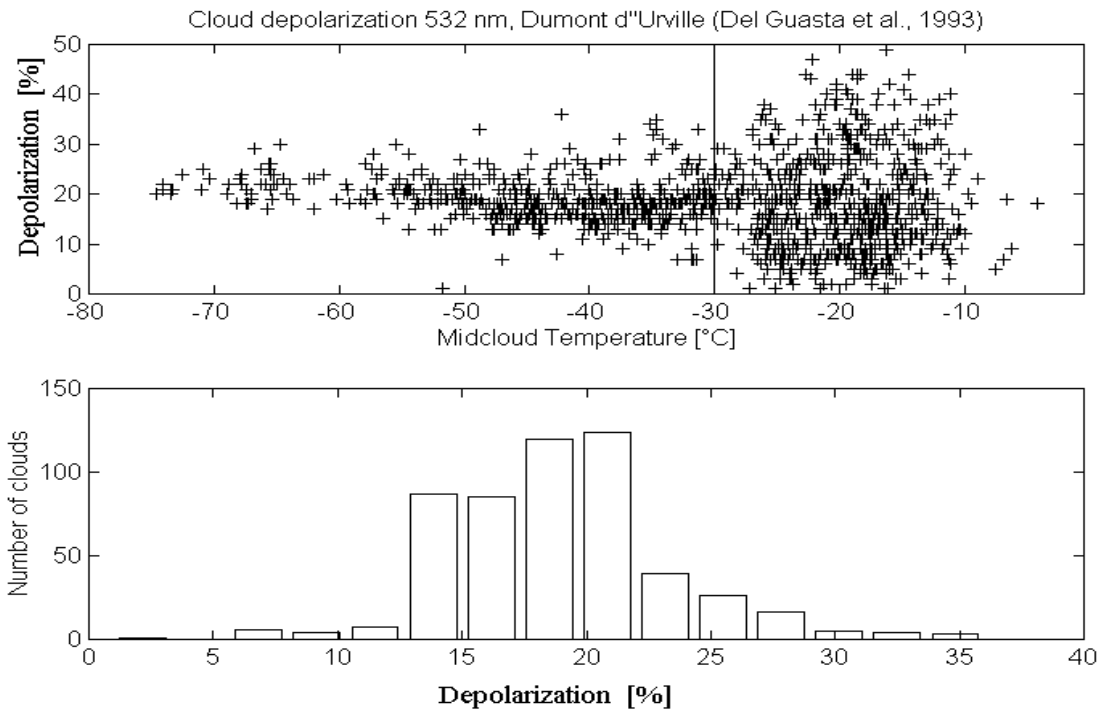

Fig.7: Statistics of δ for Antarctic cirrus (Del Guasta *et al.*,1993). The histogram was obtained for cold (midcloud temperature<-30°C) cirrus only.

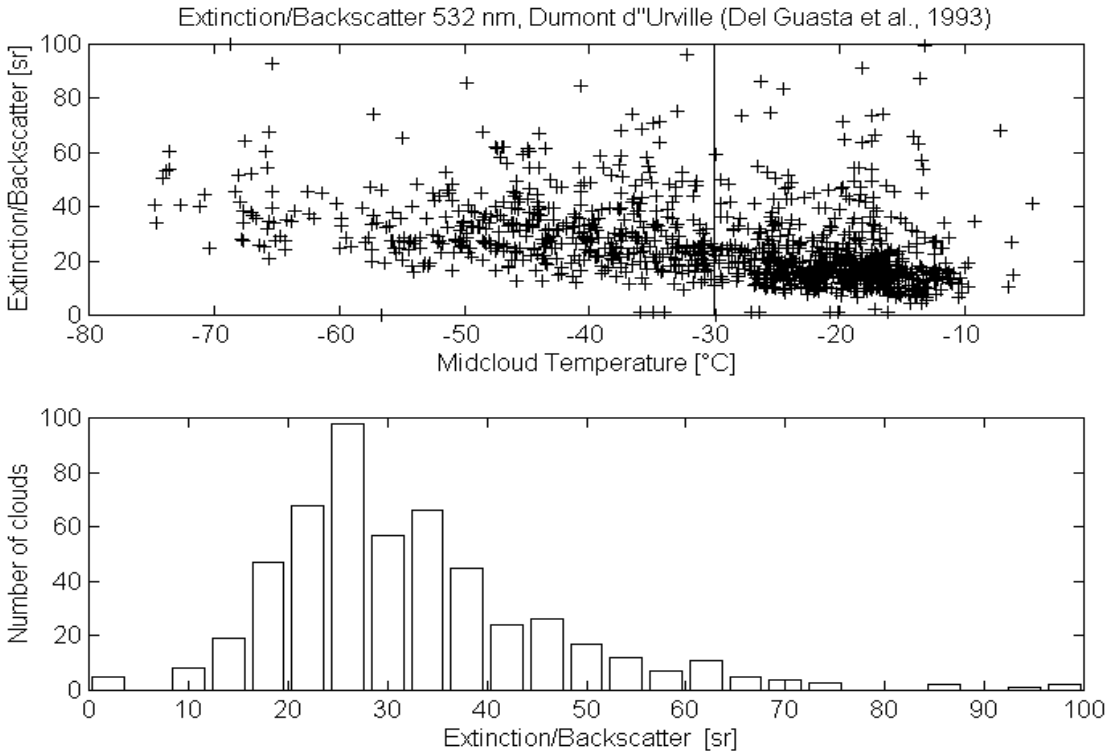

Fig. 8: Statistics of k for Antarctic cirrus (Del Guasta *et al.*,1993). The histogram was obtained for cold (midcloud temperature <-30°C) cirrus only.

The comparison of Fig.7 and Fig. 3 shows that the experimental δ is in agreement with simulated values for 100 mrad<AC<10 mrad when 0.4<AR<10. Both thick plates and columns can explain the experimental δ results. The comparison of Fig.8 and Fig.5 shows that the range of observed k values is compatible with simulations if we assume that 0.4<AR<10 and AC>10 mrad. This means that we assume that the ice particles are smaller than about 200 μm, quite a reasonable assumption, as stated in the previous paragraph. Larger particles would produce very small k values (k<10) for AR close to unit, a result incompatible with LIDAR results.

A comparison of experimental (δ, k) pairs and simulated ones for pristine crystals is shown in Fig.9. Simulations for 0.01<AR<100 are shown for different AC. (δ, k) pairs for mixtures of pristine crystals with 0.05<AR<10, and with the same total surface (and thus the same σ), were simulated by considering a number concentration comprised between 1% and 90% for each AR. Simulations were repeated for 2500 different mixtures containing random proportions of crystals with different AR. δ and k were computed as

$$\delta = \frac{\sum_i \beta_{si}}{\sum_i (\beta_{si} + \beta_{pi})} \quad \text{and} \quad k = \frac{\sum_i \sigma}{\sum_i (\beta_{si} + \beta_{pi})}$$ (the summation is extended to all the different

AR values). The centroids of the (δ, k) scatter plots obtained with the mixtures are shown in Fig.9: the mixtures of pristine crystals show (k,δ) pairs that are close to those expected for AR=1, suggesting that the LIDAR backscatter is dominated by particles with AR close to unit. Despite the variability in ice particle shapes and sizes, it is not surprising that cold polar cirrus exhibit such a narrow range of LIDAR depolarization.. Another conclusion that can be drawn from Fig.9 it is that large AC values lead to a better agreement between simulated and experimental data. It must be pointed out that some points of Fig.9, that show an almost-zero depolarization, can be attributed to the dominating presence of large plates and/or horizontally oriented crystals.

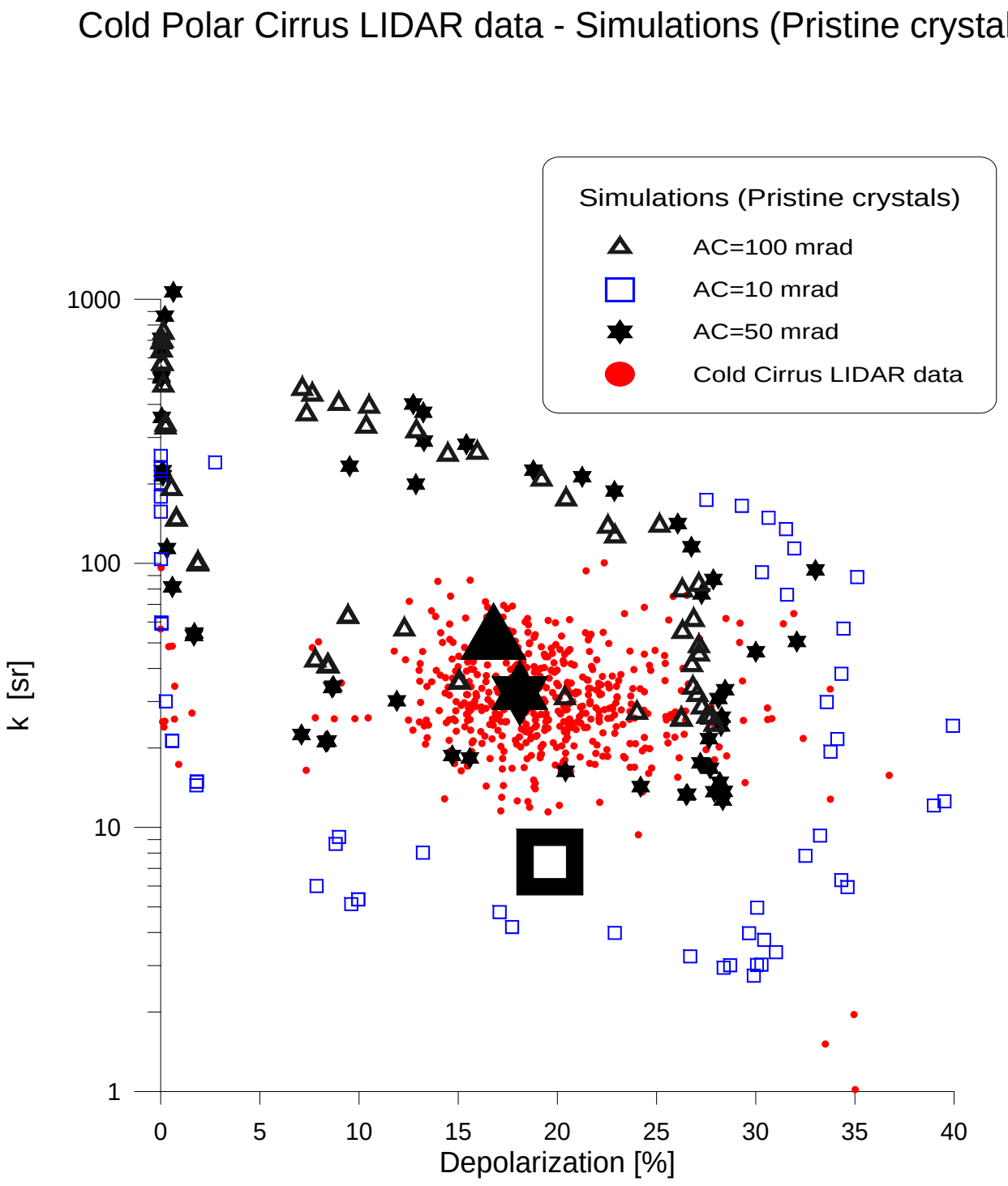

Fig.9: Comparison of (δ, k) experimental pairs for cold polar cirrus and simulations for pristine hexagonal crystals with 0.01<AR<100. The larger symbols show the centroids of the (δ, k) scatter plots expected from random mixtures of pristine crystals with 0.05<AR<10 and the same σ. The sizes of the scatter plots of the mixtures are comparable with the size of the symbols used for the corresponding centroids.

DEFORMED HEXAGONAL CRYSTALS

Pristine hexagonal crystals probably represent the equilibrium habit of ice in very stable atmospheric conditions. However, the coexistence of non-pristine crystals should be always considered, since in situ observations (Hallet, 1987; Konnen *et al.*; 1994, FIRE III) have shown the common presence of non-pristine ice crystals. Many types of irregular crystals have been used for ray-tracing studies (Peltoniemi et al., 1989; Takano and Liou, 1995; Macke, 1993; Macke et al., 1996; Macke et al., 1996; Mishchenko *et al.,* 1996). A general result from all these simulations is a reduced backscatter peak in the phase function of irregular particles compared with pristine crystals. This effect is due to the scarcity of both parallel and perpendicular faces in the irregular particles, that violates a necessary condition for a strong backscatter (Macke, 1993). LIDARs measure only the energy backscattered precisely at 180°, and thus this instrument is particularly sensitive to pristine crystals: a small quantity of these crystals could dominate the backscatter and depolarization from a cloud. A different matter is the ratio k: this quantity should increase when the number of irregular particles increases.

Since even a small deformation of the hexagonal crystals could deplete the backscatter, a simulation of the LIDAR return from a cloud composed of a mixture of pristine and slightly-deformed hexagonal crystals was performed. The goal was the interpretation of cold-cirrus LIDAR data in terms of almost-pristine hexagonal crystals.

Macke et al. (1996) and Hess *et al.* (1998) simulated the scattering from deformed hexagonal crystals by introducing a random variation in the directions of reflected and refracted rays. This is roughly equivalent to the introduction of a surface “roughness” in the crystal. In this work, ice particles are assumed to have flat, polygonal faces without roughness. Since depolarization is quite constant for pristine crystals with $1<AR<10$, a single hex column with AR=2 was used for the deformation test. Deforming columns with AR=1 produced very similar results for δ and a similar trend of k with deformation. The case of deformed thin plates was not considered, because (after some FTR tests) no significant increases of depolarization (that is, close to 0) occurred after deformation.

In this work, 6 different types of deformations were introduced:

- Type I: bullet-like deformation. The deformed particle is a truncated hexagonal pyramid, the 6 lateral faces of which are inclined by an angle α with respect to the crystal axis. α varied between 0° (pristine crystal) and 10° (Fig.10a).

-Type II: The normal vector of a top-face of the hex crystal was tilted off axis by an angle α (Fig. 10b). α varied between 0° (pristine crystal) and 10°.

-Type III: The normal vector s to both top-faces of the hex crystal were tilted off axis by an angle α, keeping the two faces parallel (Fig.10c). α varied between 0° (pristine crystal) and 10°.

-Type IV: bullet-like deformation of one lateral face only. The face was inclined by an angle α with respect to the crystal axis. α varied between 0° (pristine crystal) and 10° (Fig.10d).

-Type V: The interfacial angle between two lateral faces was changed from 60° (pristine crystal) to 90° , without changing the interfacial angles of the other faces (Fig.10e).

-Type VI: Stretching of the hexagonal section. The interfacial angle between two lateral faces was changed from 60° (pristine crystal) to 90°. The other interfacial angles were changed in order to keep all the lengths of the sides of all the faces unchanged (Fig. 10f).

Results of the FTR simulations of δ and k carried out on the 6 deformations are shown in Fig.10a to Fig.10f as functions of the increasing deformation angle α for different AC. All the deformed crystals (with the exception of type I) showed a marked backscatter peak in the phase function, making possible to extend also to these particles the approximated treatment of diffraction used for pristine crystals.

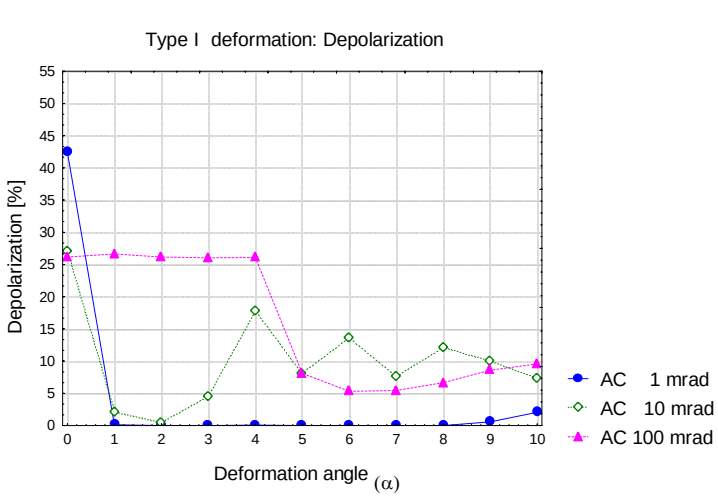

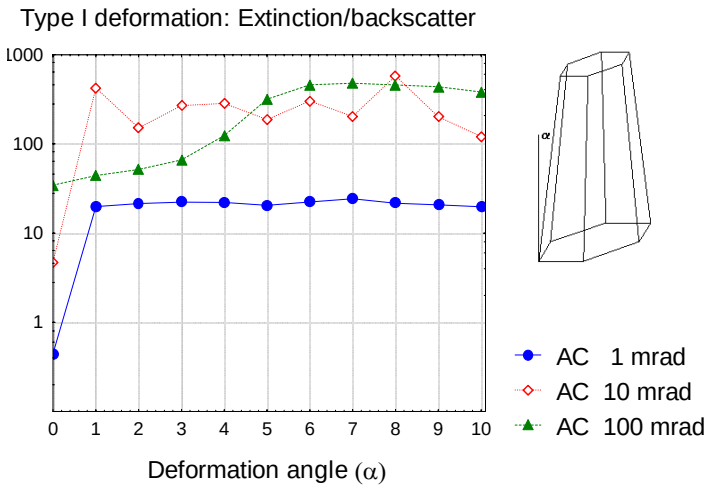

Fig 10a

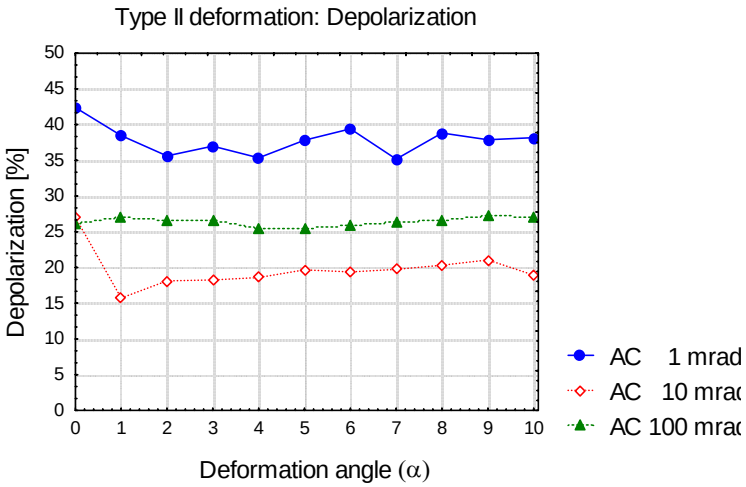

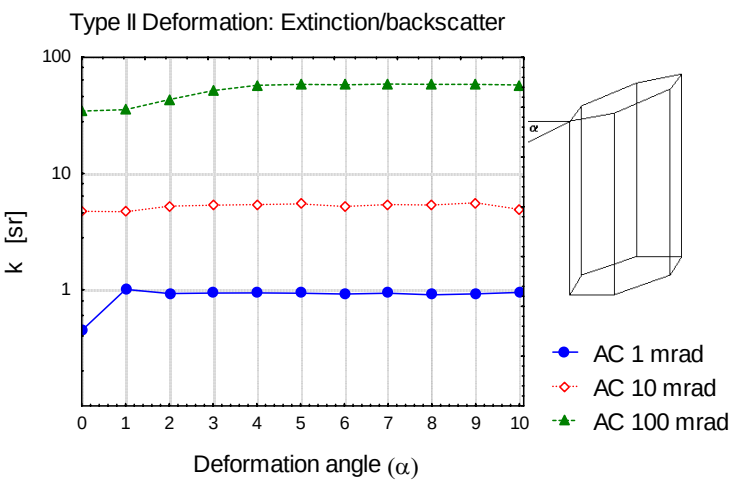

Fig 10b

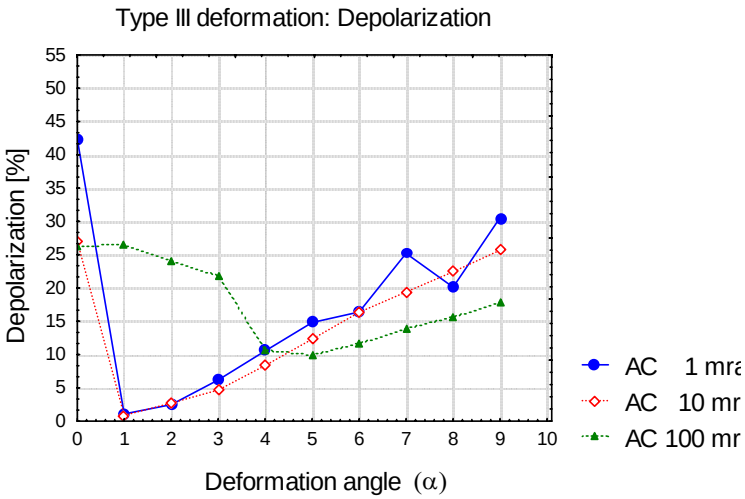

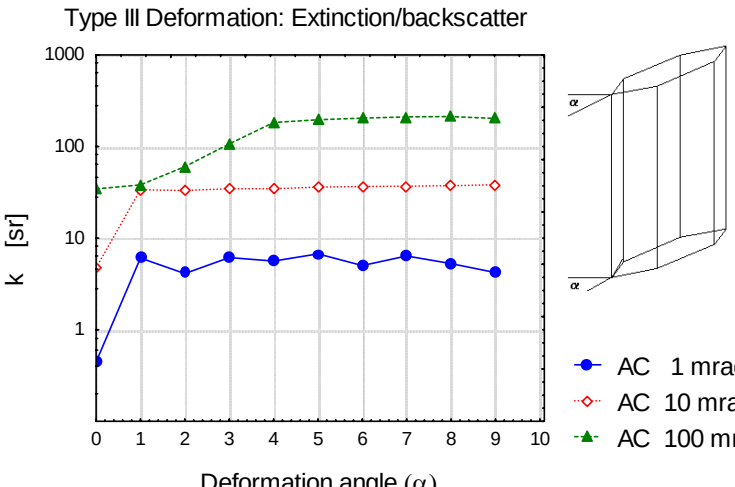

Fig 10c

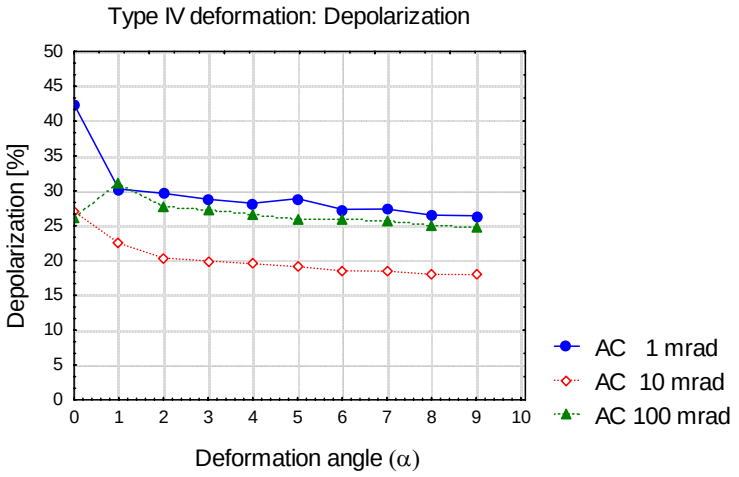

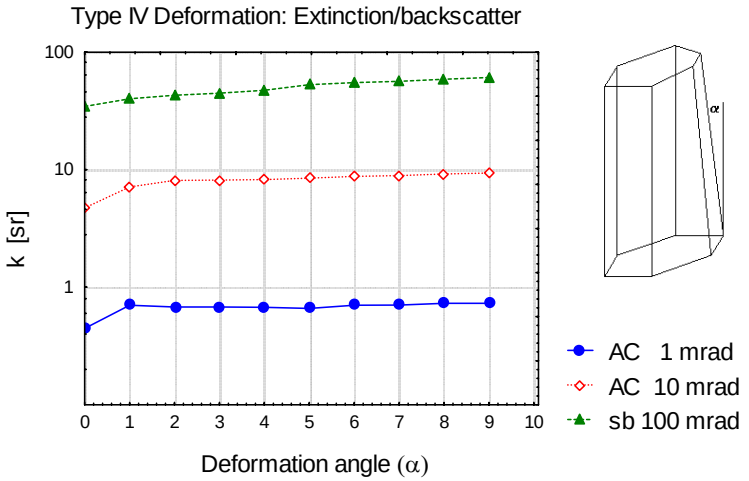

Fig 10d

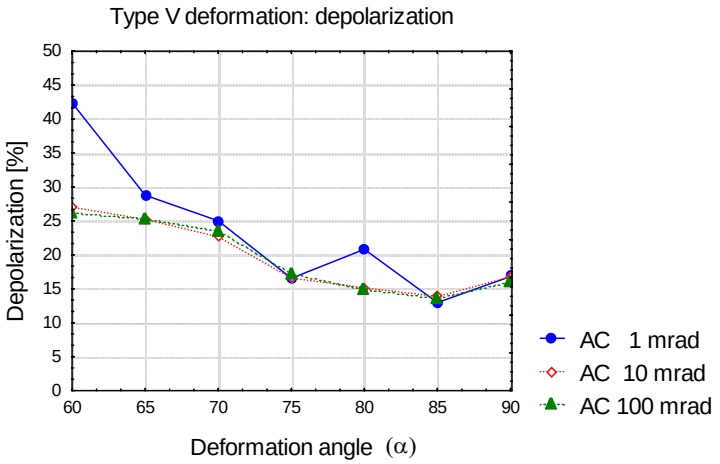

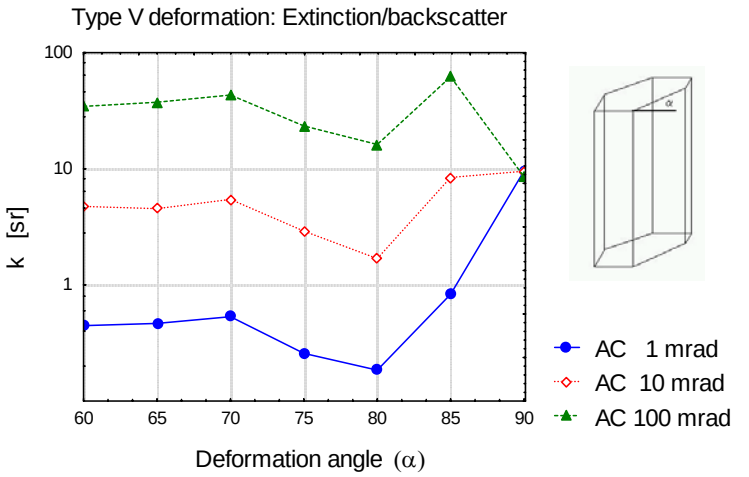

Fig 10e

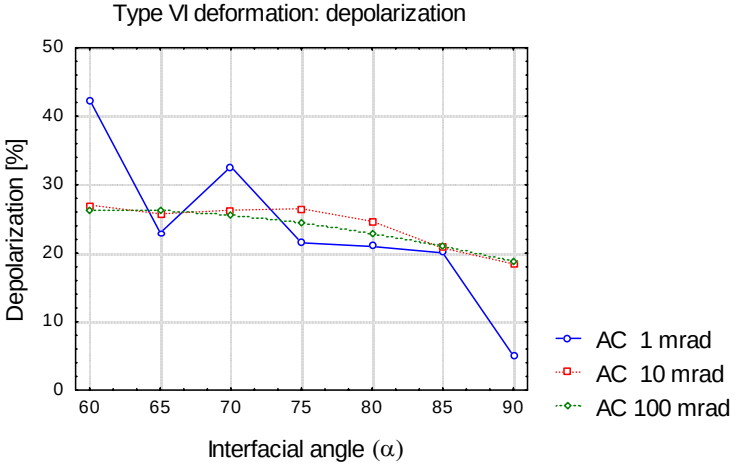

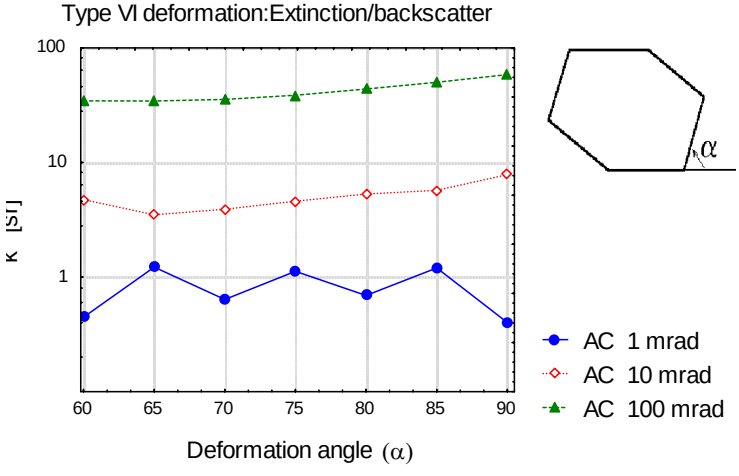

Fig 10f

δ usually decreases for any AC when the deformation is increased (sometimes it increases with increasing deformation but in nearly all cases it is smaller than in the case of pristine crystals). If the deformation affected only the crystal tips, the depolarization was almost constant (Type II) or oscillated when the deformation was increased (Type III). The case of Type II deformation is important because it shows that when one of the two tips is "pristine", δ and k are almost the same as in the case of pristine crystals, suggesting that δ and k for an ice rosette are similar to the corresponding values for a single branch.

In most deformation types, depolarization decreases with deformation much faster at small AC than at larger ones. Very small deformations (e.g. Type I) caused a dramatic decrease in depolarization to almost zero for AC<10 mrad. When the deformation was increased, an increase in k occur in most cases. In some cases (Type I and Type III), this increase can exceed a factor 10, even with very moderate deformations. The increase in k reflects the decreased backscatter, since the extinction is almost constant despite the deformation. The type V deformation produced a non-monotonic increase in k. In this case, k converged to 10 for any AC at 90° deformation (at this deformation, the deformed face became parallel to the opposite one).

The regular "Ψ" plot of pristine crystals became a very complex plot for most of the deformation types used.

The 6 deformation types used in this work obviously do not cover the possible range of slight deformations for pristine hexagonal crystals (hollow columns, some pointed columns encountered in rosettes, etc., are excluded), but they should represent a wide enough range of cases to be used for the simulation of LIDAR returns from clouds composed of almost pristine ice columns.

COMPARISON OF SIMULATIONS FOR DEFORMED CRYSTALS WITH LIDAR DATA OF COLD POLAR CIRRUS.

5000 different mixtures containing both pristine and deformed particles of the 6 types described (with all the different degrees of deformation shown in Fig.10, for a total of 52 different deformations) were simulated for AR=1.5, 10 mrad<AC<100 mrad. The number concentration of each particle type was assumed to vary random from 0 to 99% of the total particle concentration. δ and k were computed for each mixture from the

weighted sum of βp, βs, and σ of the 53 different particle types. In Fig.11 (δ,k) results are shown for the mixtures of particles in comparison with cold polar cirrus LIDAR data. Even if mixtures of pristine crystals showed (δ,k) pairs comparable to those observed in cold cirrus (Fig.9), the dispersion of LIDAR (δ ,k) data can be better explained by the presence of a mixture of pristine and deformed hex crystals. Fig.11 shows that simulations performed with AC<50 mrad do not reproduce the experimental data, while a better agreement was obtained with AC≥50 mrad. The results showed that a mixture of pristine and deformed hexagonal prisms with AR ≈1 can explain the cold cirrus LIDAR data in the hypothesis that most particles are smaller than about 100-200 μm.

The deformations introduced in this work failed to simulate the lowest depolarization data observed in cold cirrus (Fig.10,11). These data may be due to the dominating presence of plates or small subspherical particles such as those observed by Ström et al. (1993).

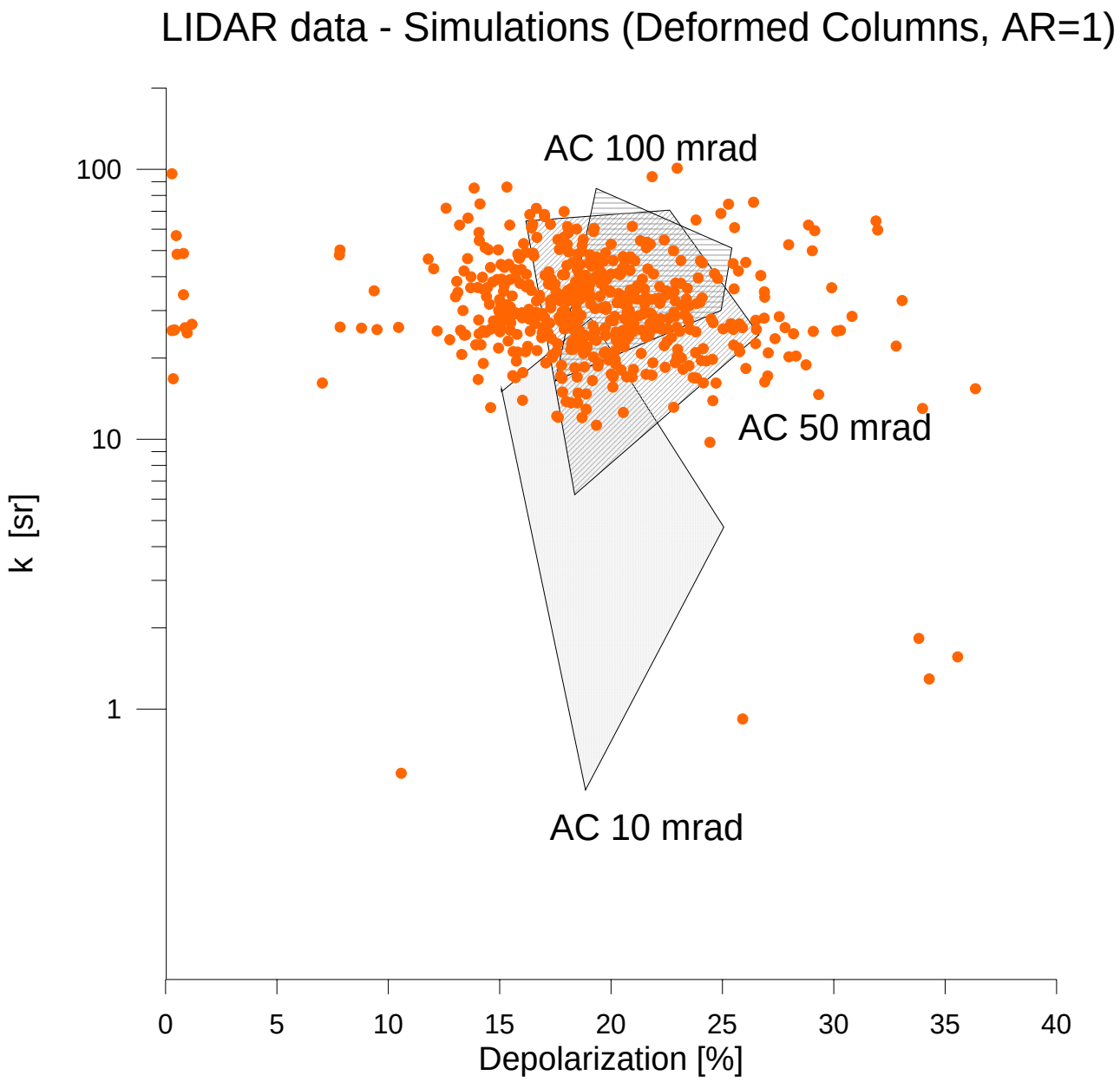

Fig.11: Comparison of experimental (δ,k) (dots) for cold cirrus and ranges of simulated (δ,k) for mixtures of pristine and deformed hexagonal crystals (see text). .

The presence of crystals different from hexagonal ones is suggested, other than by in-situ particle collections, also by the absence of 22° halos in most cirrus (unfortunately, no visual observation of halos was available for

the polar cirrus reported in this work). It should be stressed that the 22° halo is associated with the interfacial angles of the lateral faces of pristine hex crystals, and is expected also in the case of small (~10 μm) particles (Mishchenko and Macke, 1999). Introducing deformations such as Types V and VI in this work (or any other deformation changing the interfacial angles) resulted in a smoothed halo, even if the basic shape of the ice particles was still the hexagonal prism. The phase function for a mix of Type V particles with AR=2, and deformation angles between 1° and 10° shows a 22° halo weaker by a factor 4-5, compared with that of a pristine crystal. An increase in the forward and in the side-scattering was also obtained. Similar results were observed by Hess et al., (1998) as a consequence of the introduction of "surface roughness" to the pristine hex crystals. The most efficient deformation in depleting the 22° halo was Type V. Deformations of Types I and III were very efficient in the depletion of the 46° halo. It is expected that a combination of the above deformation types could result in reduced halos.

CONCLUSIONS.

Use of the FTR technique made it possible to compute δ and k at 532 nm for a wide variety of pristine and deformed hexagonal ice crystals. When the AR of pristine crystals was increased, a sharp increase in depolarization occurred near AR=1. For 1<AR<10, depolarization resulted quite constant, with a value that depended on particle size. Depolarization from pristine crystals is thus a function of both AR and crystal size: AR determines the depolarization for AR<1, while size dominates it for AR>1. The extinction/backscatter ratio k resulted size-dependent and showed a marked minimum for "compact" ice crystals (AR≈1) of any size. The different trend of δ and k with AR and particle size makes possible, in principle, the joint estimate of size and AR of populations of randomly-oriented isomorphic pristine crystals by comparing the experimental (δ, k) pairs with simulated ones (Fig.3, 5). In practice, when mixtures of pristine crystals with different AR are considered, compact particles are much more efficient backscatter centers than plates or columns with the same total surface, and their presence dominates both δ and k. For the same reason, compact particles dominate the LIDAR δ and k even in presence of large quantities of deformed hexagonal crystals. In these cases, (δ, k) pairs barely permit a rough estimate of the particle size through the size-dependency of k. From these results, it seems that the LIDAR quantities δ and k are not sensitive indicators of the cloud microphysics when "compact" pristine crystals are present in the cloud. This is apparently the case of most of

the high, cold (T<-30°C) polar cirrus shown in this work. A deviation from the δ and k values characteristic of "compact" crystals is expected only when compact, pristine hexagonal particles are practically absent.

The presence of pristine and slightly deformed crystals in clouds is associated with a narrow backscatter peak in the phase function. The backscatter computed by GO is wavelength-insensitive, but when diffraction is considered, the backscatter should show a marked $\beta(\lambda) \approx \lambda^{-1}$ behavior. Irregular particles, without backscatter peaks in the phase function, should not show such a behavior. This difference could be used as a "fingerprint" for assessing the presence of pristine/slightly deformed crystals in LIDAR signals from ice clouds. Unfortunately, a wavelength dependency $\beta(\lambda) \approx \lambda^{-1}$ and some depolarization is also expected from a wide variety of irregular small aerosols different from hexagonal crystals, and an ambiguous interpretation of multiwavelenght LIDAR data could arise. In order to solve this ambiguity, a LIDAR with a high spatial resolution could be used to check the presence/absence of the corner-reflector light peaks expected from single, almost pristine crystals.

AKNOWLEDGMENTS

I am very grateful to the Programma Nazionale di Ricerca in Antartide (PNRA) that funded this work, to Leopoldo Stefanutti, Marco Morandi and Francesco Castagnoli of the IROE LIDAR team, and to E.W. Eloranta for his suggestions.

REFERENCES

Arnott W.P., Y.Y.Dong, J. Hallett, M.R. Poellot, 1994: Role of small ice crystals in radiative properties of cirrus: a case study, FIRE II, November 22,1991. *J. of Geophys. Res*,.**99**, 1371-1381.

Auer, A.H., D.L. Veal, 1970: The dimensions of ice crystals in natural clouds. *J. Atmos. Sci.* **27**, 919-926.

Borovoi A.G., E.I. Naats, U.G. Oppel, 1999: Light backscattering by hexagonal ice crystals. Proceedings of the Tenth International Workshop on Multiple Scattering Lidar Experiments MUSCLE10, Florence (I) 19-22 April 1999, 32-47.

Cai Q., K. Liou, 1982: Polarized scattering by hexagonal ice crystals: theory, *Appl. Opt.* **21**, N19, 3569-3580.

Del Guasta M., M.Morandi, L.Stefanutti, J.Brechet, J.Piquard, 1993: One year of cloud lidar data from Dumont d'Urville: part I: general overview of geometrical and optical properties. *J. Geoph. Res.*, **98** D10, 18575-18587.

Del Guasta M., M. Morandi, L. Stefanutti, B. Stein, J. Kolenda, P. Rairoux, R. Matthey, E. Kyrö, 1994: Multiwavelength lidar observation of thin cirrus at the base of Pinatubo stratospheric layer during the EASOE campaign, *Geophys. Res. Letters*, **21**, N13, 1339-1342.

Del Guasta M., 1995: Calcolo delle proprieta' ottiche dei cristalli di ghiaccio mediante il metodo del tracciamento dei raggi. Applicazione al LIDAR a retrodiffusione. Technical Report IROE CNR, TR/GCF/95.04, pp 42

Del Guasta M., 1998: Errors in the retrieval of thin-cloud optical parameters obtained with a two-boundary algorithm. *Appl. Opt*. **37**, 5522-5540.

Del Guasta M., 1999: A second-generation ray tracing technique applied to LIDAR returns from ice clouds. Proceedings of the Tenth International Workshop on Multiple Scattering Lidar Experiments MUSCLE10, Florence (I) 19-22 April 1999, 48-57.

Hallet J., 1987: Faceted snow crystals. *J. Opt. Soc. Am.* A,**4**, 581-588.

Hess M. and M. Wiegner, 1994: COP, a data library of optical properties of hexagonal ice crystals. *Appl. Optics*, **33**, 7740-7746.

Hess M., R.B.A. Koelemeijer, P. Stammes, 1998: Scattering matrices of imperfect hexagonal ice-crystals. *J. Quant. Spectrosc. Radiat. Transfer* **60**, N3, 301-308.

Heymsfield A.J., Knollenberg R.G., 1972: Properties of cirrus-generating cells. *J. Atmos. Sci.* **29**, 1358-1366.

Heymsfield A.J., 1986: Ice particles observed in a cirriform cloud at –83°C and implications for polar stratospheric clouds. *J. of Atmos. Sci.*, **43** N8, 851-855.

Heymsfield A.J., G.M. McFarquhar, 1996: High albedo in the tropical Pacific warm pool: microphysical interpretations from CEPEX and from Kwajalein, Marshall Islands. *J. of Atmos. Sci.* **53**, N17, 2424-2451.

Iaquinta J., H. Isaka, P.Personne, 1995: Scattering phase function of bullet rosette ice crystals. *J. of Atmos. Sci*. **52**, N9, 1401-1413.

Konnen G.P., S.H.Muller, and J.Tinbergen, 1994: Halo polarization profiles and the interfacial angles of ice crystals, *App. Opt.*, **3**3, No 21, 4569-4579.

Macke A. , 1993:Scattering of light by polyhedral ice crystals, *Applied Optics*, **32**, No 15, 2781-2788.

Macke A., J. Mueller, E. Raschke, 1996: Single scattering properties of atmospheric ice crystals. *J. of Atmos. Sci*., **53** N19, 2813-2825.

McFarquhar G.M., A.J. Heymsfield, 1996: Microphysical characteristics of three anvils sampled during the Central Equatorial Pacific Experiment, *J. of Atmos. Sci.* **53**, N17, 2401-2423.

McFarquhar G.M., A.J. Heymsfield, A.Macke, J. Iaquinta, S.M.Aulenbach, 1999: Use of observed ice crystal sizes and shapes to calculate mean-scattering properties and multispectral radiances: CEPEX April 4, 1993, case study. *J. of Geophys. Res.* **104**, D24, 31763-31779.

Mishchenko M.I., W.B.Rossow, A.Macke, A.A.Lacis, 1996: Sensitivity of cirrus cloud albedo, bidirectional reflectance and optical thickness retrieval accuracy to ice particle shape. *J. of Geophys. Res*. **101**, D12, 16973-16985.

Mishchenko M.I., A.Macke, 1999: How big should hexagonal ice crystals be to produce halos? *Appl. Opt.*,**38** N9, 1626-1629.

Muinonen K., K. Lumme, W.M. Irvine, 1989: Light scattering by randomly oriented crystals. *Appl. Opt.* **28** N15, 3051-3060.

Peltoniemi J.I., K.Lumme, K.Muinonen, W.M. Irvine, 1989. Scattering of light by stochastically rough particles. *Appl. Optics,* **28** N19, 4088-4095.

Platt C.M.R., J.D. Spinhirne, W.D.Hart, 1989: Optical and microphysical properties of a cold cirrus cloud: evidence for regions of small ice particles. *J. of Geophys. Res*. **94**, D8, 11151-11164.

Pruppacher, H.R., D.J.Klett, 1985: Clouds and precipitation, D.Reidel Ed., Dordrecht, Holland, pp 714.

Sassen K., M.K. Griffin, G.C. Dodd, 1989: Optical scattering and microphysical properties of subvisual cirrus clouds, and climatic implications. *J. of Appl. Meteorol.* , 28, 91-98.

Sassen K., 1991: Corona-producing cirrus cloud properties derived from polarization lidar and photografic analysis. *Appl. Optics,* **30,** N24, 3421-3428.

Ström J., Strauss B., T.Anderson, F. Schröder F., J.Heitzenberg, P.Wendling, 1997: In situ observations of the microphysical properties of young cirrus clouds. *J. of Amos. Sci.*, **54**, 2543-2553.

Takano Y. and Jayaweera K., 1985: Scattering phase matrix for hexagonal ice crystals computed from ray optics. *Appl. Optics*, **24**, No 19, 3254-3263.

Takano Y. and K.Liou, 1989: Solar radiative transfer in cirrus clouds. Part I: single-scattering and optical properties of hexagonal ice crystals, *J. of Atmos. Sci*., **46**, No 1, 3-19.

Takano Y. and K.Liou, 1995: Radiative transfer in cirrus clouds. Part III: Light scattering by irregular ice crystals. *J. of Atmos. Sci.* **52**, N7, 818-837.

Van de Hulst H.C. (1957) *Light scattering by small particles*, J.Whiley & sons Ed., New York. pp 320.

Warren S.G., 1984: Optical constants of ice from the ultraviolet to the microwave, *Appl. Optics*, **23**, N8, 1206-1225.

Zhang J. , L. Xu, 1995: Light scattering by absorbing hexagonal ice crystals in cirrus clouds. *Appl. Optics*, **34**, N25, 5867-5874.